Article

Effect of Graphene Nanoparticles Addition on Superconductivity of YBa$_2$Cu$_3$O$_{7\sim\delta}$ Synthesized via the Thermal Treatment Method

Aliah Nursyahirah Kamarudin [1], Mohd Mustafa Awang Kechik [1,*] [ID], Siti Nabilah Abdullah [1], Hussein Baqiah [2], Soo Kien Chen [1] [ID], Muhammad Khalis Abdul Karim [1] [ID], Aima Ramli [3], Kean Pah Lim [1] [ID], Abdul Halim Shaari [1], Muralidhar Miryala [4] [ID], Masato Murakami [4] and Zainal Abidin Talib [5]

1 Department of Physics, Faculty of Science, Universiti Putra Malaysia, Serdang 43400, Selangor, Malaysia; aliahnsyahirah@gmail.com (A.N.K.); nabilahabdullah95@gmail.com (S.N.A.); chensk@upm.edu.my (S.K.C.); mkhalis@upm.edu.my (M.K.A.K.); limkp@upm.edu.my (K.P.L.); ahalim@upm.edu.my (A.H.S.)
2 Shandong Key Laboratory of Biophysics, Institute of Biophysics, Dezhou University, No. 566 University Rd. West, Dezhou 253023, China; husseinbaqiah@gmail.com
3 Department of Nanophysics, Faculty of Science and Marine Environment, Universiti Malaysia Terengganu, Kuala Nerus 21030, Terengganu, Malaysia; aima.ramli@umt.edu.my
4 Materials for Energy and Environmental Laboratory, Superconducting Materials, Shibaura Institute of Technology, 3 Chome-7-5 Toyosu, Koto, Tokyo 135-8548, Japan; miryala1@shibaura-it.ac.jp (M.M.); masatomu@shibaura-it.ac.jp (M.M.)
5 Department of Physics, College of Natural Sciences, Jeonbuk National University 567, Baekje-daero, Deokjin-gu, Jeonju-si 54896, Jeollabuk-do, Korea; zainalat@jbnu.ac.kr
* Correspondence: mmak@upm.edu.my

Abstract: The development of high-temperature superconductor (HTS) YBa$_2$Cu$_3$O$_{7\sim\delta}$ (Y123) bulks in industrial applications were established years ago. It is one of the developments that currently attracts great attention especially in transportation, superconductor cables and wires. This study is focused on the preparation of the Y123 bulk superconductors by the thermal treatment method due to the promising ways to develop high-quality Y123 superconductors with its simplicity, low cost, and relatively low reaction temperature used during the process. Y123 were added with graphene nanoparticles (x = (0.0–1.0) wt.%). Samples were then characterized by X-ray diffraction (XRD) analysis, field-emission scanning electron microscopy (FESEM), energy-dispersive X-ray spectroscopy (EDX), and alternating current susceptibility (ACS). It was found that Y123 confirmed that the majority of phases in all the XRD patterns was the orthorhombic crystal structure and the Pmmm space group with secondary phases belonged to Y$_2$Ba$_1$Cu$_1$O$_5$ (Y211). The highest T_c obtained when graphene nanoparticles were added in the Y123 sample was x = 1.0 wt.%, followed by x = 0.5 wt.% with 92.64 and 92.59 K, respectively. From the microstructure analysis, the average grain size significantly decreased to 4.754 μm at x = 0.5 wt.%. The addition of graphene nanoparticles had disturbed the grain growth of Y123, affecting the superconducting properties of the samples. On the other hand, the intergranular critical current density, J_{cm}, was found to increase with graphene nanoparticle addition and had the highest value at x = 1.0 wt.%, indicating that graphene nanoparticles acted as pinning centers in the Y123 matrix.

Keywords: Y123 superconductor; thermal treatment method; graphene nanomaterials

1. Introduction

The discovery of superconductivity in YBa$_2$Cu$_3$O$_{7\sim\delta}$ (Y123) compounds have attracted significant attention around the world due to its high critical temperature (T_c), the ability to be cooled to the superconducting state by the cheap LN$_2$ and their promising ability in numerous technological applications, including in real life such as in magnetic levitation transportations system and high power transmission cables [1–3]. Various studies have

investigated the synthesis of Y123 with different characteristics and parameters [4–11] However, many researchers are still looking to find the ideal way to produce a Y123 compound with better superconducting properties.

Despite this, the intrinsic properties of Y123 polycrystalline compounds, such as weak links at the grain boundary, have limited its performance in applications, especially at temperatures of 20–30 K and the applied magnetic field [4]. It is very challenging to raise their properties to the next level due to some limitations. This problem has been attributed to the lower J_c, which caused the degradation of its superconducting properties instead. Generally, the high superconducting performance of Y123 can be achieved by enhancing flux pinning in the Y123 system by ensuring good condition during the processing of Y123 bulks to obtain good quality and ultimate performances Y123 materials. The Y123 superconductor materials are well known for their best performance, especially in reaching higher magnetic field trapping [2]. With the higher trapped fields, these materials can be used as strong magnets for trapped field applications. The enhancement in the capability of field trapping depends on its dimension and its critical current density, J_c.

Several studies have reported that significant improvements of critical current density (J_c) could be obtained through the addition of impurities or nanomaterials in various forms [12–21]. These impurities and additions of nanomaterials act as the flux pinning centers in HTS could help prevent the motion of magnetic flux in the Y123 compounds, thus leading to high J_c under the applied magnetic field. The artificial and strong pinning centers are required in order to achieve high J_c [14,22–24]. In recent years, some studies found that the addition of carbon-based compounds improved intergrain connectivity.

Consequently, the value of J_c had increased, since these nanoparticles act as artificial pinning centers [25]. For instance, De Silva et al. found that graphene-doped MgB_2 superconductors had significantly improved superconducting properties [26]. Dadras et al. reported that the addition of graphene oxide up to $x = 0.7$ wt.% in the Y123 compound significantly plays a role as an intergrain weak link to enhance flux pinning and J_c of the Y123 mixture [27]. For instance, the interconnected particles were formed with less porosity when graphene oxide was added into the YBCO materials [28]. These studies proved that the J_c and flux pinning of superconductor materials could be enhanced with these graphene additions in the Y123.

Various combinations of these graphene materials have been reported in technology applications and studies [28–31]. Many studies have shown their usefulness especially in electronics, photocatalysis and photovoltaic devices such as in enhancing Raman scattering (SERS) detection and electrochemical detections [32–34]. Graphene is known as one of the carbon-based nanomaterials composed of a two-dimensional (2D) hexagonal lattice with special properties, such as high surface area, good electrical conductivity and better thermal conductivity, which may help to be effective in pinning centers in current-carrying capability to improve the J_c values [35–37].

Following up the motivation from the previous study, it is interesting to study the effects of graphene additions towards the J_c values and pinning force of Y123 bulk. Hence, this study is focused on studying the effects of graphene nanoparticles on the crystal structure, phase formation of Y123 phase and superconducting properties, T_c and J_{cm} values of Y123 compounds via the thermal treatment method with the addition of $x = 0.01$ wt.%, 0.3 wt.%, 0.5 wt.% and 1.0 wt.% graphene nanoparticles. Other than that, the preparation of Y123 added with graphene nanoparticles is yet to be implemented in the preparation of superconductor materials. Thus, one of the focuses of this study is to perform the thermal treatment method for Y123 added with graphene nanoparticles.

2. Materials and Methods

Y123 samples were prepared using the thermal treatment method [20]. Metal nitrate, yttrium (III) nitrate hydrate $Y(NO_3)_3 \cdot 6H_2O$ (99.99%), barium nitrate, $Ba(NO_3)_2$ (99.95%) and copper (II) nitrate hemi-(pentahydrate) $Cu(NO_3)_2 \cdot 2.5H_2O$ (98.0%) from Alfa Aesar were weighed with a ratio of 1:2:3 stoichiometric amounts and dissolved in a 2% aqueous solution PVP, $(C_8H_9NO)_n$, which acts as a capping agent to minimize the agglomeration of particles and solvents [38]. The metal nitrate and the polymer solution were mixed and constantly stirred for 2 h with 850 rpm at 80 °C until it turns into a slightly blue solution. The mixed solution was poured into the glass petri dish and dried in an oven for 24 h at 110 °C to evaporate the water until a solid-like green gel is formed.

Then, the gel obtained was crushed using a mortar and pestle until it formed a fine powder, after which pre-calcination of the powder was conducted at 600 °C for 4 h. The pre-calcined powder was reground and calcined again at 910 °C for 24 h with slow cooling air at the rate of 1 °C/min to room temperature. The powdered samples obtained from the calcination process were added with graphene sheets (99.99%, Nanostructured and Amorphous Materials, Inc. Houston, TX, USA) with a mean diameter of 0.5~3 μm and thickness of 0.55–1.2 nm at x = 0.0 wt.%, 0.1 wt.%, 0.3 wt.%, 0.5 wt.% and 1.0 wt.%. Then, the powdered mix was reground using an agate mortar until it was well-mixed and pressed into circular pellets of 13 mm diameter and 5 mm thickness. Finally, the pellets were sintered at 980 °C for 24 h with the flowing of oxygen gas and then cooled slowly to room temperature in a furnace at a rate of 1 °C/min.

The thermal decomposition behavior of the Y123 metal nitrate precursor powders were analyzed using a Mettler Toledo thermogravimetric analyzer (model TGA/SDTA851^e, Mettler Toledo, Zürich, Switzerland) to heat up to 1000 °C with the heating rate 10 °C/min and nitrogen as a purge gas with 50 mL/min. Samples obtained were analyzed using X-ray diffraction (XRD, Xpert Pro Panalytical Philips DY 1861 diffractometer, Phillip, Eindhoven, The Netherlands) with Cu K_α radiation for the structural analysis of phase formation and crystal structure. The surface microstructure of the samples was observed by field-emission scanning electron microscope (FESEM) JSM-7100F (JEOL, Tokyo, Japan) EDS and EBSD. In addition, the superconducting magnetic properties of critical temperature, T_c and critical current J_{cm} were measured using the AC-Susceptibility (ACS) spectrometer (Cryobind, Zagreb, Crotia).

3. Results and Discussions

3.1. Thermogravimetric Analysis (TG/DTG)

Figure 1 shows the thermal decomposition of uncalcined Y123 metal nitrate precursor powder from 50 to 1000 °C in nitrogen gas with a 5°/min scanning rate. The drops could be associated with the proper particular sintering temperature. The sample exhibits four drops of the degradation process. The first drop of the 12.39% weight loss starting at around 50 °C can be attributed to the moisture loss and water evaporation. This process can be seen clearly by the DTG measurements, where gradual loss of moisture occurred. The several decompositions and degradations with significant weight loss of 59.23% took place from 190 °C, and were related to the decomposition of some gases and organic matter and polymer such as CO_2 and PVP, as seen in the DTG curve. The next drop at a range of 350–597 °C showed the exothermic peak represents the decomposition of the remain volatile products and the weight of samples turns practically constant [39]. On the fourth drop, it can be seen that the weight loss became insignificant due to PVP content in the sample turned to a carbonaceous product, and left pure metal oxide as the final residue [40]. From the DTG curve, the trend of increasing temperature at around 850 °C indicates the formation of YBCO single crystal has begun for the final pure product sample. At a temperature above 930 °C, the formation of a Y123 single crystal was produced with an orthorhombic structure. Thus, the appropriate heating temperature range was obtained for calcination and sintering temperature.
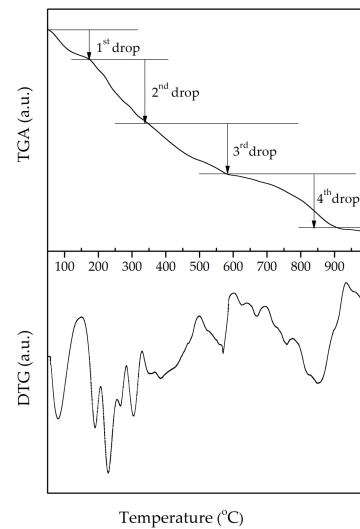
Figure 1. Thermogravimetric (TG/DTG) curves analysis of uncalcined Y123 powder.

3.2. X-ray Diffraction Analysis

The XRD patterns of pure Y123 and Y123 added with graphene nanoparticle, where x = 0.0 wt.%, 0.1 wt.%, 0.3 wt.%, 0.5 wt.% and 1.0 wt.% samples are shown in Figure 2a. The data were analyzed by X'Pert Highscore Plus software with the Rietveld refinement and ICSD database. This figure confirms that all samples are dominant by a single phase of Y123 (ICSD No. 98-004-1823) with the P*mmm* symmetry space group. The highest peak of the major phase Y123 was approximately observed at $2\theta = 32.84°$ with (110) planes that indicate all samples were constantly in the orthorhombic phase. The presence of a few secondary phases, such as Y211 (ICSD No. 98-002-8780) observed at $2\theta = 29.84°$, $30.56°$ and $47.56°$ with plane orientation (*hkl*) of (211), (112) and (512) respectively, has increased with the addition of graphene nanoparticles. The Y211 non-superconducting phase have been detected in all samples as minor peaks that are commonly observed in the Y123 superconductors as secondary phases. Even so, graphene nanoparticle reflections were not observed in the analysis of all samples due to the small values of x = wt.% used, which cannot be detected during the characterizations [22].

(a)
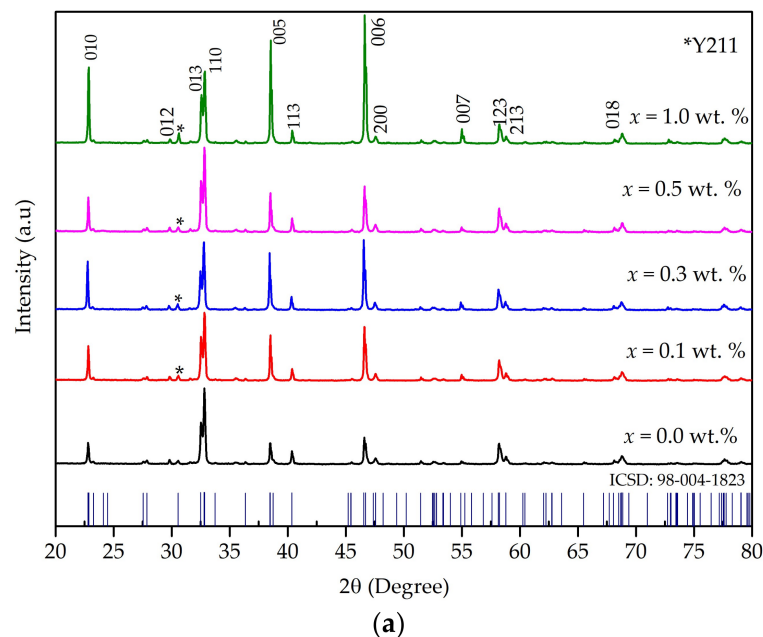
Figure 2. *Cont.*
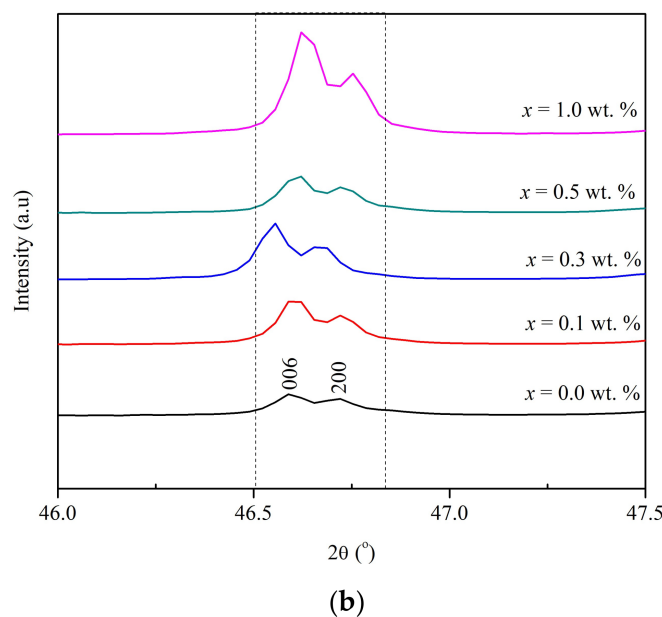
Figure 2. (**a**) X-ray diffraction analysis of Y123 added with graphene nanoparticles by the thermal treatment method. (**b**) The XRD patterns of the peaks corresponding to the (006) and (200) plane of the Y123 peaks in the Y123 + *x* wt.% graphene nanoparticles.

Nevertheless, it can be seen that the intensity peak of the Y123 phase decreased with the increase of graphene additions that may be due to the interference in the composite sample by carbon atoms, as shown in Figure 2b up to $x = 0.5$ wt.% at the twin peak $2\theta \approx 46.75°$ and $47.55°$. The fact that graphene consists of carbon atoms that function to create the tension in the superconducting grains has led to the changes of the peak position, including the intensity of the phases of the samples [36,40]. Despite the slight change of intensity in the samples, a Rietveld analysis confirmed that all samples were in the P*mmm* space group. Table 1 shows the lattice parameter, unit cell volume and crystallite size of the samples. From the table, it was observed that the crystallite size obtained varied with the addition of graphene nanoparticles. However, samples with $x = 0.5$ wt.% showed the smallest value of 73.68 nm compared with the pure sample $x = 0.0$ wt.% with 103.65 nm, respectively. This is supported by a previous literature review, which mentioned that the addition of nanoparticle impurities promoted a better crystal structure of Y123 [27,41].

It was found that the lattice parameters for all samples changed with regard to the addition of graphene nanoparticle content in Y123 samples. It can be seen that the lattice parameters a, b and c for samples $x = 0.3$ wt.% decreased compared to the other samples. This is supported by the reduction of the intensity when the graphene nanoparticles increased. It can be concluded that graphene nanoparticles do not enter the Y123 crystal lattice and may be left between the Y123 grains [42,43]. The orthorhombic structure of the Y123 phase was calculated using the (a−b)/(a+b) formula and is listed in Table 1. The changes in lattice parameters resulted in the increase of the orthorhombic structure at $x = 0.3$ wt.% but decrease upon the addition of graphene nanoparticles up to $x = 0.5$ wt.% and 1.0 wt.%. The changes with variation of lattice parameters (a, b, c) were observed. However, the orthorhombic structures were conserved similar to the pure samples and no orthorhombic-to-tetragonal transition occurred for all samples after the oxygenation.

Table 1. Lattice parameters of a, b and c axes, unit cell volume, crystallite size and orthorhombicity of Y123 + *x* wt.% graphene nanoparticles.

Samples (wt.%)	a (Å)	b (Å)	c (Å)	V^3 (Å^3)	Crystallite Size (nm)	Orthorhombicity Factor
0.0	3.8213 ± 0.0002	3.8812 ± 0.0002	11.6784 ± 0.0005	173.21	103.65	0.0078
0.1	3.8209 ± 0.0002	3.8817 ± 0.0002	11.6787 ± 0.0004	173.21	125.72	0.0079
0.3	3.8197 ± 0.0002	3.8813 ± 0.0002	11.6769 ± 0.0004	173.11	103.65	0.0080
0.5	3.8219 ± 0.0002	3.8818 ± 0.0002	11.6777 ± 0.0004	173.25	73.68	0.0078
1.0	3.8235 ± 0.0002	3.8817 ± 0.0003	11.6794 ± 0.0004	173.34	182.50	0.0076

3.3. Surface Morphology of FESEM Analysis

To further understand the role of graphene in the microstructure morphology of Y123 samples, an FESEM analysis was carried out. All sample images were viewed with 1000× magnification. The average grain size was calculated using Image-*J* software by taking around 100 selected grains from the FESEM images as listed in Table 2. From the analysis, as shown in Figure 3a–e, it was observed that the pure sample has an irregular shape distributed randomly and formed more strongly compacted with structures with less porosity. However, changes in the grain sizes were observed along with the presence of porosity with the increase of graphene nanoparticles. The average grain size obtained for samples *x* = 0.0 wt.%, 0.1 wt.%, 0.3 wt.%, 0.5 wt.% and 1.0 wt.% were 6.38, 4.54, 5.52, 4.75 and 8.92 μm, respectively. The average grain size of pure Y123 sample decreased from 6.38 μm to 4.75 for sample *x* = 0.5 wt.%. However, at *x* = 1.0 wt.%, the average grain size showed an increase of up to 8.92 μm with closely packed grain formation and decreased porosity between the grains. The addition of graphene nanoparticles increased the grain size with closely packed formation, promoting grain growth and contributing to the intergranular transport currents [44]. Regardless, sample *x* = 0.5 wt.% showed a slight porosity caused by the loosely packed formation between superconducting grains resulting in low grain connectivity. The reduction in the grain connectivity disrupted the grain growth, weakened the flux pinning and limited the J_c values.

Table 2. The average grain sizes, *D* of the Y123 with additions of graphene.

Samples (wt.%)	Average Grain Sizes *D* (μm)
0.0	6.384 ± 0.33
0.1	4.539 ± 0.22
0.3	5.524 ± 0.25
0.5	4.754 ± 0.24
1.0	8.916 ± 0.69

(a)

(b)
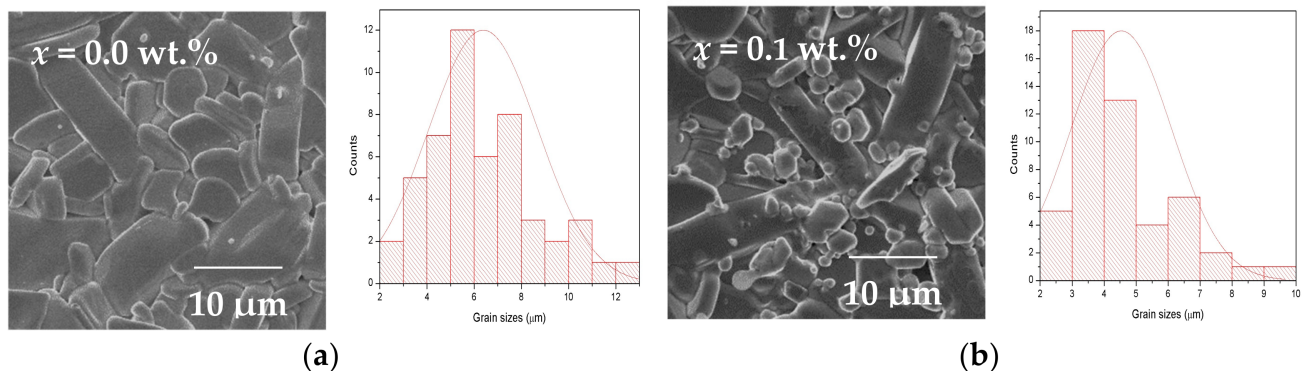
Figure 3. *Cont.*
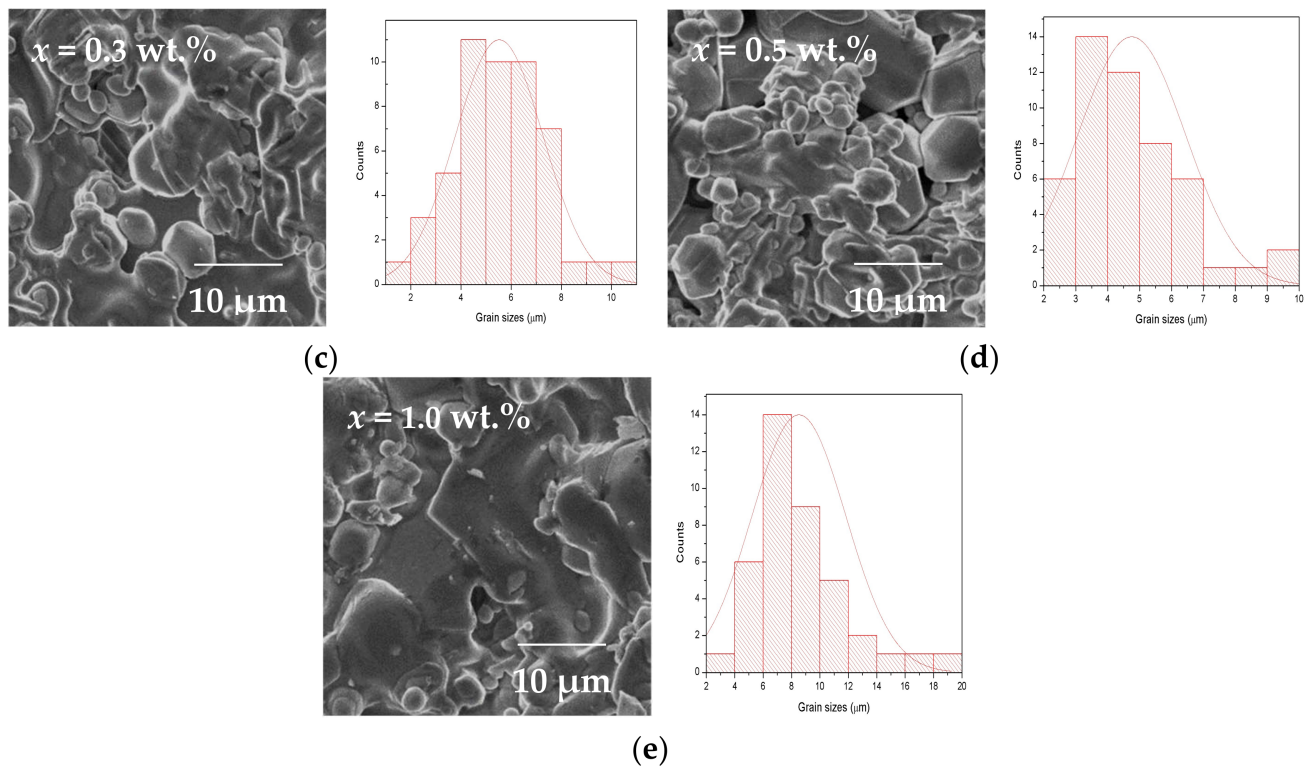
Figure 3. (**a–e**) FESEM images and histogram of average grains of Y123 with various additions of graphene nanoparticles measured from image *J* software under $1000\times$ magnification.

EDX analysis was performed on random spot grain analysis of the compounds. The atomic ratios observed for all samples were close to the 1:2:3 ratio of Y:Ba:Cu except for $x = 0.5$ wt.% samples. The increase of the atomic ratio for Y elements may be due to porosity, as shown in Figure 4. It was found that the composition of carbon elements was detected in all samples added with a percentage value around 4.47%–13.31%. The distribution of the graphene (C) element in Y123 can be seen from the EDX elemental mapping of C ions precipitates and histogram shown in Figures 4 and 5 for the samples $x = 0.5$ wt.% and 1.0 wt.%, respectively. The result indicated that the C element was present in the Y123 samples even though it was not observed from the XRD spectra because the size was too small to be detected by XRD measurement. The atomic percentage of carbon elements observed were increased from 4.47% to 13.31% in samples $x = 0.1$ wt.% and $x = 1.0$ wt.%, respectively. This shows that the addition of graphene in the Y123 samples increased with the increase of the graphene nanoparticles contents, which shows a good agreement with a previous study [45].

3.4. AC Susceptibility Analysis

The superconducting transition temperature, T_c, was obtained from the magnetization measurement method using AC susceptibility. Figure 6 shows the graph analysis plotted with χ' and χ'' versus temperature at a frequency of $f = 219$ Hz under an AC magnetic field of 0.5 Oe. In HTS, the appearance of the double-step transition in χ' followed by two loss peaks in χ'' is always present in the characteristic feature of AC susceptibility. In the real part χ', $T_{c\text{-onset}}$ is correlated to the intragranular transition. In contrast, the second transition T_{cj} is related to the coupling matrix due to the superconducting coupling of intergranular properties [46]. Meanwhile, in the imaginary part, χ'', it has been noticed that the peak temperature, T_p, shows maximum energy loss caused by the full penetration in the samples. The T_p shifted to a lower temperature and the peak became broad when it dropped to zero. $T_{p\text{-inter}}$ and $T_{p\text{-intra}}$ ($T_{p\text{-inter}} < T_{p\text{-intra}}$) showed maximum hysteresis loss due to the motion of intergranular Josephson and intragranular (Abrikosov) vortices, respectively [47].
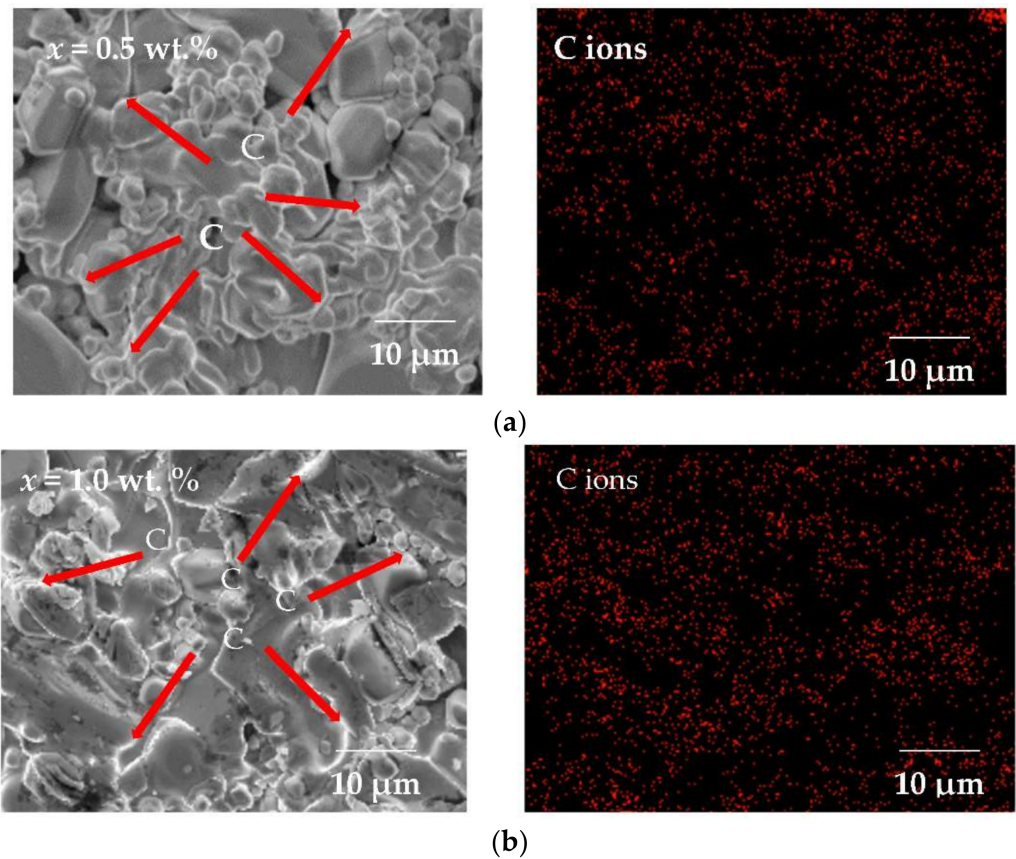
Figure 4. FESEM images and EDX mapping C ions (red dots) of the compound Y123 added with graphene nanoparticles up to (**a**) x = 0.5 wt.% and (**b**) 1.0 wt.%, indicating the presence of the expected elements.
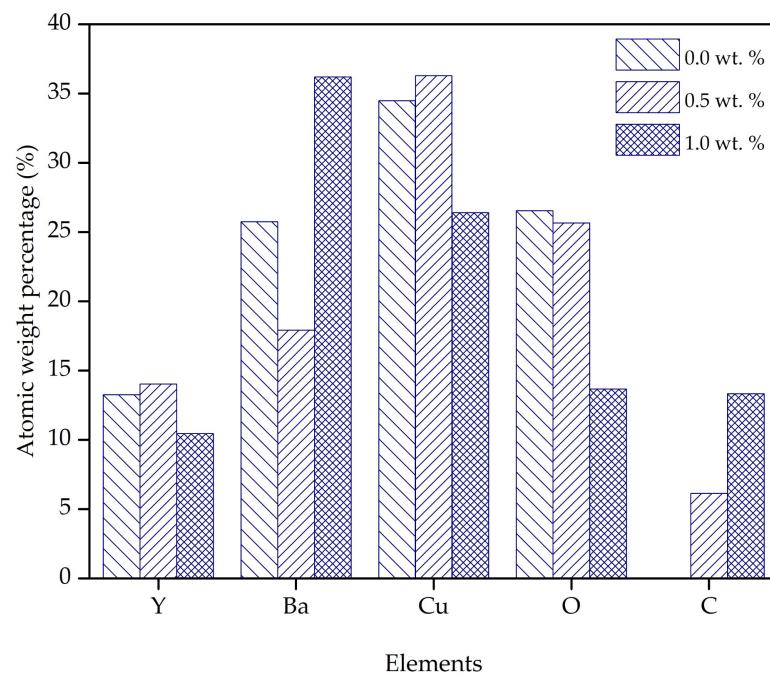
Figure 5. Histogram of average weight percentages of pure Y123 and Y123 added with graphene nanoparticles up to x = 1.0 wt.% from the EDX analysis.

The broad or narrow separation of the intra- and intergranular dissipation peaks signifies the connection among the grains and whether it has good/bad connections. From Figure 6, the single-step diamagnetic transition was seen in a pure sample of Y123 that differ from the appearance of double-step diamagnetism for all samples added with graphene nanoparticles from $x = 0.1$ wt.%–1.0 wt.%. The value of T_c decreased from 92.65 to 92.30 K when $x = 0.1$ wt.% graphene nanoparticles were added. However, the T_c slowly increased up to 92.64 K with $x = 1.0$ wt.% graphene nanoparticles. The high T_c obtained may be due to the improvement of oxygen deficiency in the Cu-O chain.

For the imaginary part, χ'', the T_p observed were 89.77, 91.84, 88.89, 89.31 and 91.69 K for samples $x = 0.0$ wt.%, 0.1 wt.%, 0.3 wt.%, 0.5 wt.%, and 1.0 wt.%, as shown in Table 3. However, T_p is broadened and shifted to the lower temperature with the increase of graphene nanoparticles in Y123 samples due to the weakening of intergranular coupling between grains, as shown in Figure 4 [48]. This decrement may be due to some defects at the grain boundaries such as grain disorientation, twin boundaries and vacancies that can act as weak links, therefore disturbing the T_p and pinning forces [49]. The broad width of χ'' might also be caused by the second superconducting transition of the secondary phase. However, T_p in the intergranular properties was seen in samples $x = 0.1$ wt.% and 1.0 wt.% because intra- and intergranular peaks were closely located. However, the broadened and shifted T_p to the low temperature with increase in graphene nano addition weakened the grain coupling, thus weakening the pinning force.
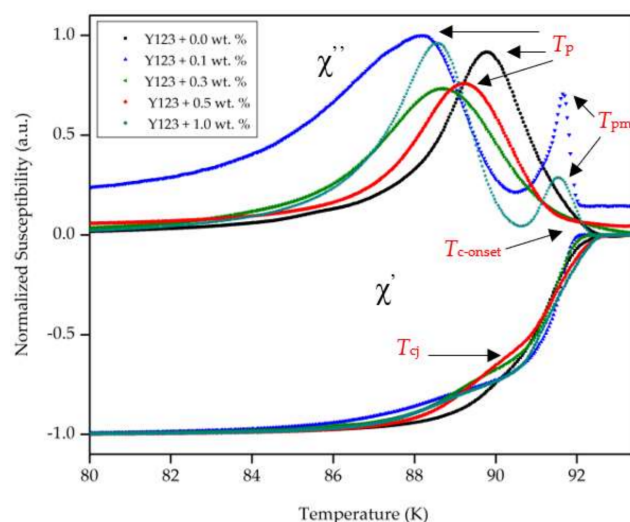
Figure 6. The real (χ') and imaginary part (χ'') of the AC susceptibility for Y123 under AC magnetic field of 0.5 Oe and frequency 219 Hz. The real part of samples shifted to the lower temperature up to 92.30 K for sample $x = 0.1$ wt.%.

In addition, the maximum values of losses at T_p of χ'' applied field have been extracted as a full penetration field when the flux line penetrated the center of samples. The Bean Model is employed to determine the intergranular current density, J_{cm}. A rectangular bar-shaped sample with cross-section 2a × 2b is defined as follows:

$$J_{cm}\left(T_p\right) = \frac{Hac}{(ab)^{1/2}} \tag{1}$$

where H_{ac} is the amplitude of the applied AC field. Table 3 lists the values of J_{cm} at the applied magnetic field of 0.5 Oe for the samples. The highest J_{cm} value was achieved for sample $x = 1.0$ wt.% with 25.94 A/cm^2 as compared to the pure samples. This enhancement could be supported by the microstructure result shown in the FESEM analysis. The formation of a good connection between grains has strengthened this, thus improving the intergranular coupling of Y123. Such improvement could be convincingly introduced into

the high pinning performance of the Y123 samples, as it was affected by a good source of pinning sites, which was the addition of graphene nanoparticles. The graphene nanoparticles can be a powerful material to act as an as effective pinning center. These findings were supported from the previous studies that had also reported that graphene/carbon base nanomaterials addition could be beneficial, especially in the Y123 superconductor performance [24,36,49,50]. However, further improvements of the Y123 superconducting performance are possible in order to obtain more higher of J_{cm} values. From the result, the I_o values can be estimated using the Ambegaokar-Baratoff theory, shown in the equation below [51]:

$$I_o \; = \; 1.57 \; \times \; 10^{-8} \; \times \; \left(\frac{T_{c-onset}{}^2}{T_{conset} - T_{cj}}\right) \tag{2}$$

The results calculated are tabulated in Table 3, which shows that Josephson's current increased drastically up to 114.32 μA for sample $x = 0.1$ wt.%. However, the I_o value dropped with the increase of graphene nanoparticles from $x = 0.3$ wt.% to 1.0 wt.%. The I_o obtained for all samples showed a very slight difference among the values. These results explain that introducing graphene nanoparticles weakens grain coupling inside the material that causes decreased Josephson current flow across grain boundaries [50].

Table 3. Onset critical temperature, $T_{c\text{-onset}}$, phase lock-in temperature, T_{cj}, coupling temperature, T_p, critical current density, J_{cm} and Josephson current, I_o of the Y123 added with graphene nanoparticles samples in AC field of 0.5 Oe.

Samples (wt.%)	$T_{c\text{-onset}}$ (K)	T_{cj} (K)	T_p (K)	J_{cm} (A/cm^2)	I_o (μA)
0.0	92.65	-	89.77	24.16	1.465
0.1	92.30	91.13	91.84	22.87	114.32
0.3	92.50	90.92	88.89	19.60	85.02
0.5	92.59	90.83	89.31	21.29	76.47
1.0	92.64	90.78	91.69	25.94	72.44

4. Conclusions

In conclusion, Y123 superconductors with $x = 0.0$ wt.%, 0.1 wt.%, 0.3 wt.%, 0.5 wt.% and 1.0 wt.% have been successfully prepared by the thermal treatment method. The XRD analysis using Rietveld refinement showed that Y123 major phase was found with orthorhombic structures and the secondary phase of Y211 in all samples, even though the XRD analysis cannot detect the presence of graphene nanoparticles. However, the EDX analysis showed that the graphene nanoparticles were well distributed in all samples added with graphene nanoparticles. For sample $x = 0.5$ wt.%, the structure becomes porous, causing the calculated J_{cm} to decrease. From the AC susceptibility analysis, the broadening of the intergranular peaks had caused the weakening of the grain coupling. The addition of graphene nanoparticles had improved the I_o. It is noted that the $x = 0.1$ wt.% sample exhibited the highest T_{cj}, with 91.13 K, and has the highest maximum Josephson current, I_o, of 114.32 μA as compared to the other samples. Finally, the critical current density, J_{cm} was higher in samples $x = 1.0$ wt.% compared to the pure sample. This shows that graphene nanoparticles act as pinning centers that improved the enhancement of the J_{cm}.

Institutional Review Board Statement: Not applicable.

Informed Consent Statement: Not applicable.

Data Availability Statement: The data presented in this study are available on request from the corresponding author. The data are not publicly available due to ethical restrictions.

Conflicts of Interest: The authors declare no conflict of interest.

References

1. Paranthaman, M.P.; Izumi, T. High-performance YBCO-coated superconductor wires. *MRS Bull.* **2004**, *29*, 533–537. [CrossRef]
2. Deng, Z.; Izumi, M.; Miki, M.; Tsuzuki, K.; Felder, B.; Liu, W.; Zheng, J.; Wang, S.; Wang, J.; Floegel-Delor, U.; et al. Trapped flux and levitation properties of multiseeded YBCO bulks for HTS magnetic device applications-part II: Practical and achievable performance. *IEEE Trans. Appl. Supercond.* **2012**, *22*, 6800210. [CrossRef]
3. Werfel, F.N.; Floegel-Delor, U.; Riedel, T.; Goebel, B.; Rothfeld, R.; Schirrmeister, P.; Wippich, D. Large-scale HTS bulks for magnetic application. *Phys. C Supercond. Appl.* **2013**, *484*, 6–11. [CrossRef]
4. Koblischka-Veneva, A.; Koblischka, M.R.; Ide, N.; Inoue, K.; Muralidhar, M.; Hauet, T.; Murakami, M. Microstructural and magnetic analysis of a superconducting foam and comparison with IG-processed bulk samples. *J. Phys. Conf. Ser.* **2016**, *695*, 012002. [CrossRef]
5. Muralidhar, M.; Kenta, N.; Zeng, X.L.; Koblischka, M.R.; Diko, P.; Murakami, M. Record critical current densities in IG processed bulk $YBa_2Cu_3O_y$ fabricated using ball-milled $Y_2Ba_1Cu_1O_5$ phase. *Phys. Status Solid Appl. Mater. Sci.* **2016**, *213*, 443–449.
6. Ramli, A.; Shaari, A.H.; Baqiah, H.; Kean, C.S.; Kechik, M.M.A.; Talib, Z.A. Role of Nd_2O_3 nanoparticles addition on microstructural and superconducting properties of $YBa_2Cu_3O_{7-\delta}$ ceramics. *J. Rare Earths* **2016**, *34*, 895–900. [CrossRef]
7. Dihom, M.M.; Shaari, A.H.; Baqiah, H.; Kechik, M.M.A. Effects of calcination temperature on microstructure and superconducting properties of y123 ceramic prepared using thermal treatment method effects of calcination temperature on microstructure and superconducting properties of Y123 ceramic prepared using. *Solid State Phenom.* **2017**, *268*, 325–329. [CrossRef]
8. Hapipi, N.M.; Chen, S.K.; Shaari, A.; Kechik, M.M.A.; Tan, K.B.; Lim, K.P. Superconductivity of Y_2O_3 and $BaZrO_3$ nanoparticles co-added $YBa_2Cu_3O_{7-\delta}$ bulks prepared using co-precipitation method. *J. Mater. Sci. Mater. Electron.* **2018**, *29*, 18684–18692. [CrossRef]
9. Arlina, A.; Karim, Y.; Chen, S.K.; Halim, S.A.; Kechik, M.M.A. Synthesis and effect of Al_2O_3 added in yttrium barium copper oxide $YBa_2Cu_3O_\delta$ by solid state reaction method. *J. Trop. Resour. Sustain. Sci.* **2016**, *4*, 75–77.
10. Yusuf, N.N.M.; Kechik, M.M.A.; Baqiah, H.; Chen, S.K.; Lim, K.P.; Shaari, A.A.; Jusoh, W.N.W.W.; Sukor, S.I.A.; Dihom, M.M.; Talib, Z.A.; et al. Structural and superconducting properties of thermal treatment-synthesised bulk $YBa_2Cu_3O_{7-\delta}$ superconductor: Effect of addition of SnO_2 nanoparticles. *Materials* **2019**, *12*, 92. [CrossRef] [PubMed]
11. Kamarudin, A.N.; Kechik, M.M.A.; Muralidhar, M.; Pinmangkorn, S.; Murakami, M.; Chen, S.K.; Baqiah, H.; Ramli, A.; Lim, K.P.; Halim, S.A. Microstructural, phase formation, and superconducting properties of bulk $YBa_2Cu_3O_y$ superconductors grown by infiltration growth process utilizing the $YBa_2Cu_3O_y$ + $ErBa_2Cu_3O_y$ + $Ba_3Cu_5O_8$ as a liquid source. *Coatings* **2021**, *11*, 377. [CrossRef]
12. Haugan, T.; Barnes, P.N.; Wheeler, R.; Meisenkothen, F.; Sumption, M.; Melsenkothen, F.; Sumption, M. Addition of nanoparticle dispersions to enhance flux pinning of the $YBa_2Cu_3O_{7-x}$ superconductor. *Nature* **2004**, *430*, 867–870. [CrossRef] [PubMed]
13. Dadras, S.; Gharehgazloo, Z. Effect of Au nano-particles doping on polycrystalline YBCO high temperature superconductor. *Phys. B Phys. Condens. Matter* **2016**, *492*, 45–49. [CrossRef]
14. Baqiah, H.; Halim, S.A.; Chen, S.K.; Lim, K.P.; Kechik, M.M.A. Effects of rare earth nanoparticles (M = Sm_2O_3, Ho_2O_3, Nd_2O_3) addition on the microstructure and superconducting transition of $Bi_{1.6}Pb_{0.4}Sr_2Ca_2Cu_3O_{10+\delta}$ ceramics. *Sains Malays.* **2016**, *45*, 643–651.
15. Mikheenko, P.; Abell, J.S.; Sarkar, A.; Dang, V.S.; Kechik, M.M.A.; Tanner, J.L.; Paturi, P.; Huhtinen, H.; Babu, N.H.; Cardwell, D.A.; et al. Self-assembled artificial pinning centres in thick YBCO superconducting films. *J. Phys. Conf. Ser.* **2010**, *234*, 022022. [CrossRef]
16. Hapipi, N.M.; Chen, S.K.; Halim, S.A.; Kechik, M.M.A.; Tan, K.B.; Lim, K.P.; Lee, O.J. AC susceptibility of $BaZrO_3$ nanoparticles added $YBa_2Cu_3O_{7-\delta}$ superconductor prepared via coprecipitation method. *J. Supercond. Nov. Magn.* **2019**, *32*, 1191–1198. [CrossRef]

17. Mikheenko, P.; Sarkar, A.; Dang, V.S.; Tanner, J.L.; Kechik, M.M.A.; Abell, J.S.; Crisan, A. Pinning centers induced in YBCO films by nano-dots in substrate decoration and quasi-superlattice approaches. *IEEE Trans. Appl. Supercond.* **2009**, *19*, 3491–3494. [CrossRef]

18. Abd-Shukor, R.; Kechik, M.M.A.; Halim, S.A. Transport critical current density of Bi-Sr-Ca-Cu-O/Ag superconductor tapes with addition of Fe_3O_4 as flux pinning center. *J. Phys. Conf. Ser.* **2008**, *97*, 2–8. [CrossRef]

19. Arlina, A.; Halim, S.A.; Kechik, M.M.A.; Chen, S.K. Superconductivity in Bi-Pb-Sr-Ca-Cu-O ceramics with YBCO as additive. *J. Alloys Compd.* **2015**, *645*, 69–273. [CrossRef]

20. Dihom, M.M.; Halim, S.A.; Baqiah, H.; Al-Hada, N.M.; Chen, S.K.; Azis, R.S.; Kechik, M.M.A.; Talib, Z.A.; Abd-Shukor, R. Microstructure and superconducting properties of Ca substituted $Y(Ba_{1-x}Ca_x)_2Cu_3O_{7-\delta}$ ceramics prepared by thermal treatment method. *Results Phys.* **2017**, *7*, 407–412. [CrossRef]

21. Dihom, M.M.; Halim, S.A.; Baqiah, H.; Al-Hada, N.M.; Talib, Z.A.; Chen, S.K.; Azis, R.S.; Kechik, M.M.A.; Lim, K.P.; Abd-Shukor, R. Structural and superconducting properties of $Y(Ba_{1-x}K_x)_2Cu_3O_{7-\delta}$ ceramics. *Ceram. Int.* **2017**, *43*, 11339–11344. [CrossRef]

22. Khalid, N.A.; Kechik, M.M.A.; Baharuddin, N.A.; Chen, S.K.; Baqiah, H.; Yusuf, N.N.M.; Halim, S.A.; Hashim, A.; Talib, Z.A. Impact of carbon nanotubes addition on transport and superconducting properties of $YBa_2Cu_3O_{7-\delta}$ ceramics. *Ceram. Int.* **2018**, *44*, 9568–9573. [CrossRef]

23. Dou, S.X.; Soltanian, S.; Horvat, J.; Wang, X.L.; Zhou, S.H.; Ionescu, M.; Liu, H.K.; Munroe, P.; Tomsic, M. Enhancement of the critical current density and flux pinning of MgB_2 superconductor by nanoparticle SiC doping. *Appl. Phys. Lett.* **2002**, *81*, 3419–3421. [CrossRef]

24. Khalid, N.A.; Kechik, M.M.A.; Baharuddin, N.A.; Chen, S.K.; Baqiah, H.; Lim, K.P.; Halim, S.A.; Talib, Z.A.; Hashim, A.; Murakami, M.; et al. Carbon nanofibers addition on transport and superconducting properties of bulk $YBa_2Cu_3O_{7-\delta}$ material prepared via co-precipitation. *J. Mater. Sci. Mater. Electron.* **2020**, *31*, 16983–16990. [CrossRef]

25. Lee, C.Y.; Kao, Y.H. Frequency dependence of the intergranular energy-loss peak in AC magnetic susceptibility of high-T_c superconductors. *Phys. C Supercond.* **1996**, *256*, 183–190. [CrossRef]

26. De Silva, K.S.B.; Xu, X.; Gambhir, S.; Wang, X.L.; Li, W.X.; Wallaceb, G.G.; Doua, S.X. Flux pinning mechanisms in graphene-doped MgB_2 superconductors. *Scr. Mater.* **2011**, *65*, 634–637. [CrossRef]

27. Dadras, S.; Dehghani, S.; Davoudiniya, M.; Falahati, S. Improving superconducting properties of YBCO high temperature superconductor by Graphene Oxide doping. *Mater. Chem. Phys.* **2017**, *193*, 496–500. [CrossRef]

28. Colie, M.; Mihaiescu, D.; Surdu, A.; Trusca, R.; Vasile, B.; Istrati, D.; Ficai, A.; Plapcianu, C.; Andronescu, E. High temperature superconducting materials based on Graphene/YBCO nanocomposite. *Mater. Today Proc.* **2016**, *3*, 2628–2634. [CrossRef]

29. Kong, W.; Kong, I.; Kechik, M.M.A.; Abd-Shukor, R. Effect of graphene addition on the transport critical current density of bulk $(Tl_{0.8}5Cr_{0.15})Sr_2CaCu_2O_{7-\delta}$ superconductor. *Mater. Today Proc.* **2018**, *5*, 3176–3184. [CrossRef]

30. Justh, N.; Berke, B.; László, K.; Bakos, L.P.; Szabó, A.; Hernádi, K.; Szilágyi, I.M. Preparation of graphene oxide/semiconductor oxide composites by using atomic layer deposition. *Appl. Surf. Sci.* **2018**, *453*, 245–251. [CrossRef]

31. Akilarasan, M.; Kogularasu, S.; Chen, S.M.; Chen, T.W.; Lin, S.H. One-step synthesis of reduced graphene oxide sheathed zinc oxide nanoclusters for the trace level detection of bisphenol A in tissue papers. *Ecotoxicol. Environ. Saf.* **2018**, *161*, 699–705. [CrossRef]

32. Cançado, L.G.; Jorio, A.; Ferreira, E.H.M.; Stavale, F.; Achete, C.A.; Capaz, R.B.; Moutinho, M.V.O.; Lombardo, A.; Kulmala, T.S.; Ferrari, A.C. Quantifying defects in graphene via Raman spectroscopy at different excitation energies. *Nano Lett.* **2011**, *11*, 3190–3196. [CrossRef] [PubMed]

33. Parvathi, V.P.; Parimaladevi, R.; Sathe, V.; Umadevi, M. Environmental photochemistry by plasmonic semiconductor decorated GO nanocomposites: SERS detection and visible light driven degradation of aromatic dyes. *Appl. Surf. Sci.* **2019**, *473*, 864–872. [CrossRef]

34. Ng, Y.H.; Iwase, A.; Bell, N.J.; Kudo, A.; Amal, R. Semiconductor/reduced graphene oxide nanocomposites derived from photocatalytic reactions. *Catal. Today* **2011**, *164*, 353–357. [CrossRef]

35. Kogularasu, S.; Govindasamy, M.; Chen, S.M.; Akilarasan, M.; Mani, V. 3D graphene oxide-cobalt oxide polyhedrons for highly sensitive non-enzymatic electrochemical determination of hydrogen peroxide. *Sens. Actuators B Chem.* **2017**, *253*, 773–783. [CrossRef]

36. Sahoo, B.; Routray, K.L.; Samal, D.; Behera, D. Effect of artificial pinning centers on YBCO high temperature superconductor through substitution of graphene nano-platelets. *Mater. Chem. Phys.* **2019**, *223*, 784–788. [CrossRef]

37. Pei, S.; Cheng, H.M. The reduction of graphene oxid. *Carbon* **2012**, *50*, 3210–3228. [CrossRef]

38. Naseri, M.G.; Saion, E.B.; Hashim, M.; Halim, S.A.; Ahangar, H.A. Synthesis and characterization of zinc ferrite nanoparticles by a thermal treatment method. *Solid State Commun.* **2011**, *151*, 1031–1035. [CrossRef]

39. Melnikov, P.; Nascimento, V.A.; Consolo, L.Z.Z.; Silva, A.F. Mechanism of thermal decomposition of yttrium nitrate hexahydrate, $Y(NO_3)_3 \cdot 6H_2O$ and modeling of intermediate oxynitrates. *J. Therm. Anal. Calorim.* **2013**, *111*, 115–119. [CrossRef]

40. Jasim, S.E.; Jusoh, M.A.; Hafiz, M.; Jose, R. Fabrication of Superconducting YBCO Nanoparticles by Electrospinning. *Procedia Eng.* **2016**, *148*, 243–248. [CrossRef]

41. Lui, C.H.; Liu, L.; Mak, K.F.; Flynn, G.W.; Heinz, T.F. Ultraflat graphene. *Nature* **2009**, *462*, 339–341. [CrossRef]

42. Sheahen, T. *Introduction to High-Temperature Superconductivity*; Springer Science & Business Media: Berlin, Germany, 1994.

43. Wei, K.; Ing, K.; Hamdan, M.S.; Radiman, S. AC Susceptibility and superconducting properties of graphene added YBa$_2$Cu$_3$O$_{7-d}$. *J. Supercond. Nov. Magn.* **2018**, *31*, 2699–2703. [CrossRef]

44. Dadras, S.; Falahati, S.; Dehghani, S. Effects of graphene oxide doping on the structural and superconducting properties of YBa$_2$Cu$_3$O$_{7-\delta}$. *Phys. C Supercond. Appl.* **2018**, *548*, 65–67. [CrossRef]

45. Parinov, I.A. *Microstructure and Properties of High-Temperature Superconductors*; Springer: Berlin/Heidelberg, Germany, 2007.

46. Hannachi, E.; Almessiere, M.A.; Slimani, Y.; Baykal, A.; Ben Azzouz, F. AC susceptibility investigation of YBCO superconductor added by carbon nanotubes. *J. Alloys Compd.* **2016**, *812*, 152150. [CrossRef]

47. Ramli, A.; Halim, S.A.; Chen, S.K.; Kechik, M.M.A. The effect of Gd$_2$O$_3$ nanoparticles addition on microstructural and electrical properties of YBCO superconductor. *ARPN J. Eng. Appl. Sci.* **2016**, *11*, 13708–13715.

48. Sharma, D.; Kumar, R.; Awana, V.P.S. DC and AC susceptibility study of sol-gel synthesized Bi$_2$Sr$_2$CaCu$_2$O$_{8+\delta}$ superconductor. *Ceram. Int.* **2013**, *39*, 1143–1152. [CrossRef]

49. Sarmago, R.V.; Singidas, B.G. Low field AC susceptibility of YBCO: The frequency and field dependence of intra- and intergrain coupling losses in the absence of vortices. *Supercond. Sci. Technol.* **2004**, *17*, S578. [CrossRef]

50. Peng, J.; Liu, Y.; Ma, Z.; Shahriar Al Hossain, M.; Xin, Y.; Jin, J. Superior critical current density obtained in MgB$_2$ bulks via employing carbon-coated boron and minor Cu addition. *Phys. C Supercond. Appl.* **2016**, *528*, 60–64. [CrossRef]

51. Ambegaokar, V.; Baratoff, A. Tunneling between superconductors. *Phys. Rev. Lett.* **1963**, *11*, 104. [CrossRef]